Journal of Nuclear Materials 510 (2018) 524–538

Contents lists available at ScienceDirect

Journal of Nuclear Materials

journal homepage: www.elsevier.com/locate/jnucmat

Characterization of crystallographic texture of Zirconium alloy components by neutron diffraction

F. Malamud [a], A. Moya Riffo [a], M.A. Vicente Alvarez [a], P. Vizcaino [b], M.J. Li [c], X. Liu [c], S.C. Vogel [d], M. Law [e], V.V. Sumin [f], V. Luzin [e], R.N. Vasin [f], J.R. Santisteban [a, *]

[a] Centro Atómico Bariloche, CNEA/CONICET, Bariloche, 8400, Argentina
[b] Centro Atómico Ezeiza, CNEA/CONICET, Ezeiza, Argentina
[c] China Advanced Research Reactor, CIAE, Beijing, 102413, China
[d] Material Science and Technology Division, Los Alamos National Laboratory, Los Alamos, NM, 87545, USA
[e] ANSTO, Lucas Heights, NSW, 2232, Australia
[f] FLNP JINR, Dubna, 141980, Russian Federation

ARTICLE INFO

Article history:
Received 18 June 2018
Received in revised form
3 August 2018
Accepted 4 August 2018
Available online 8 August 2018

ABSTRACT

The reproducibility of the determination of crystallographic texture of Zr-based components by neutron diffraction has been studied through a small round-robin exercise, with the participation of texture and residual stress diffractometers from five international laboratories. Both constant-wavelength and polychromatic neutron beams have been used to define the texture of specimens from a warm-rolled and annealed Zircaloy-4 plate, and from a Zr-2.5%Nb pressure tube. Measurements were also compared to synchrotron high energy X-ray diffraction experiments, as a complementary volumetric technique with much shorter data collection times compared to neutrons. Results are qualitatively consistent and reproducible in terms of pole figures and orientation distribution function, underlining the suitability of neutrons for bulk texture measurements. Expected uncertainty of measurements has been quantified by global parameters such as texture indexes and Kearns factors, and local parameters associated to the main texture components (volume fraction, centroids, and widths of fiber components). The typical uncertainties found for these parameters are compared to spatial differences found in a small batch of cold-rolled Zr-2.5%Nb pressure tubes.

1. Introduction

Internal structural components of nuclear power reactors such as fuel channels and fuel assemblies are made of Zirconium (Zr) alloys, due to an excellent combination of good mechanical properties, corrosion resistance and very low neutron absorption. Pure Zr has a hexagonal *hcp* crystal structure up to 865 °C (α phase when it transforms into a cubic *bcc* structure (high temperature β phase). Zr is alloyed to improve its mechanical and corrosion properties. Zircaloy-2 and Zircaloy-4 are the most popular alloys, used for the fabrication of fuel elements in the Western world, with tin and iron as the main alloying elements. Zr-Nb alloys are used in fuel elements of Russian reactors and in high burn-up Western reactors, as well as in structural components of CANDU and Indian Pressurized Heavy Water Reactors (PHWR). In all cases, Zr alloys are used mostly in the form of tubes and plates produced by conventional metallurgical procedures.

Due to the elastic and plastic anisotropy of the Zr hexagonal structure, components made of Zr alloys commonly present grain structures with preferential orientation, as a result of the several thermo-mechanical processes involved during manufacturing [1,2]. This preferential crystallite orientation is usually termed crystallographic texture and it is quantified by means of the orientation distribution function (ODF) of the material. The crystallographic texture and the type, density and distribution of crystalline defects resulting from manufacturing, impact not only on the mechanical properties of the material, but also on other degradation mechanisms that occur in-service [3,4].

In nuclear power plants Zr-based components are in contact with coolant water at ~300 °C (and ~100 atm pressure). The coolant water slowly oxidizes their surface, and a small fraction of the

* Corresponding author.
E-mail address: j.r.santisteban@gmail.com (J.R. Santisteban).

https://doi.org/10.1016/j.jnucmat.2018.08.003
0022-3115/

Hydrogen (H) produced in the reaction is steadily absorbed by the component. H in excess of the solid solubility precipitates as a fragile hydride phase that limits the service life of the component. The orientation of hydride precipitates determines the susceptibility to crack failure, and it is strongly influenced by the crystallographic texture and by the spatial distribution of the plastic deformation introduced during manufacturing [5–8].

In service, Zr alloys are also exposed to high doses of radiation that create microscopic defects. The evolution of such defects over long periods of time results in a distortion of the shape of structural components. Creep and *irradiation growth* are strongly influenced by the impurity content, crystallographic texture and the type and density of dislocations within the component. For Zr alloy pressure tubes under many years in service, this gives an expansion in length and diameter, and a small reduction in thickness [3].

Hence crystallographic texture characterization is paramount for defining operational performance of pressure tubes and the crystallographic texture in hexagonal materials, and in Zr alloy tubing in particular, is specified by design and controlled after manufacturing. Most research and characterization of Zr alloy textures is traditionally performed from experimental pole figures measured using laboratory X-rays diffractometers, and a round robin exercise has determined standard practices and variability characteristic of this technique [9]. Neutron diffraction has also been used to study and characterize texture on Zr alloys. Although not as widely available as X-rays and with comparatively much lower fluxes, neutron beams offer some important features for the non-destructive characterization of textures. Due to their high penetration, bulk textures can be measured with minimal sample preparation required [10], an important advantage for the investigation of irradiated specimens after long times in service [11]. Besides this, materials science neutron diffractometers are usually furnished with stress rigs and furnaces [12], which allow monitoring texture changes that occur during thermo-mechanical treatments, as a result of phase transformations [13] [14] or large microstructural changes [15–19]. Finally, the spatial resolution available at neutron strain scanners is an attractive option for non-destructive studies of texture variation across specimens [20–22].

By contrast to laboratory X-ray diffractometers, neutron diffractometers are unique instruments that are designed and optimized to each particular neutron source, usually a nuclear reactor or a particle accelerator. Instruments exist with a variety of detector and collimator arrangements, using either monochromatic or white neutron beams. In all cases, the characterization of crystallographic texture is based on measuring the intensity of a large number of diffraction peaks at selected angles and determining the orientation distribution function (ODF) of the crystallites composing the sample from least-squares fits to these pole figures [23] by using different software packages [24–26].

This work presents a round robin exercise on texture of Zr alloys by neutron diffraction. A previous neutron texture round robin on a weakly-textured calcite sample was conducted [27], however, the difficulties occurring in practice with the stronger textures found in Zr alloys, as well as the advances in analysis software, neutron sources, and instrumentation warrant the present round robin. This work is an extension of a round robin exercise [28] developed as part of a Coordinated Research Project (CRP) organized by the International Atomic Energy Agency (IAEA) on Development, Characterization and Testing of Materials of Relevance to Nuclear Energy Sector Using Neutron Beams. A preliminary report of the work can be found in Ref. [29].

The principal objective of this work is to validate the measurement strategies for texture determination of Zr alloys at several neutron diffractometers. Besides this, we are also interested in estimating the standard uncertainty to be expected for the Kearns factors and other integral parameters of Zr alloys ODFs obtained from neutron diffractometers. Finally, as neutron beam time is always scarce and some studies deal with only minor changes in texture, we want to assess the quality of the information obtained from incomplete measurements of pole figures in Zr alloy tubing.

Bulk and local texture measurements were performed at five different international neutron laboratories on specimens produced from a rolled Zircaloy-4 plate and a Zr2.5%Nb pressure tube, yet not all laboratories measured all specimens. The neutron diffraction results were compared to companion experiments performed with high energy synchrotron X-ray diffraction (HE-XRD), a similar volumetric technique with much higher sample throughput that allows finer coverage of the pole figure.

2. Samples

2.1. Zircaloy-4 plates

The first set of samples consisted of small coupons machined from a warm-rolled and annealed Zircaloy-4 plate of 6.25 mm thickness, produced by Wah Chang, USA (ASTM B352, Grade R60804), with dimensions of 10 mm and 7 mm along the transverse (TD) and rolling directions (RD), respectively. A complete microstructural characterization of this plate has been presented in Ref. [30]. It has the classical equiaxed grain structure of annealed rolled plates, with diameters ranging from 10 μm to 20 μm. This microstructure is very similar to that of the Zircaloy-4 materials used in fuel cladding. Fig. 1-(a) shows a polarized light image of the warm-rolled Zircaloy-4 plate across the normal-transverse plane, where each grain orientation is represented by a different colour. The ODF has been measured in detail by HE-XRD experiments at the 1-ID beamline of APS, USA [14], and Fig. 1-(c) shows an ODF plotted as a 3D surface, using Bunge rotation convention (consequtive rotations around axes Z, X, Z of the sample coordinate system by angles $\varphi_1, \Phi, \varphi_2$, respectively) [31]. Considering a hexagonal crystal symmetry, the three-dimensional space of possible orientations is reduced to: $0 \leq \varphi_1 \leq 360^{\circ}$, $0 \leq \Phi \leq 90^{\circ}$, $0 \leq \varphi_2 \leq 60^{\circ}$. The crystallographic texture of the plate is typical of cold rolled and recrystallized Zircaloy-4, with a large proportion of grains having their *c*-axis rotated ~35° from the normal direction (ND) to the transverse direction (TD), and either their (10–10) and (11–20) plane normal pointing along the rolling direction (RD), as schematically represented in Fig. 1-(b). As seen in Fig. 1-(c), two symmetrically reflected fiber-like textures with fiber axes at $,\Phi \sim 35^{\circ}$, $\varphi_1 = 0^{\circ}$ and $\Phi \sim 35^{\circ}$, $\varphi_1 = 180^{\circ}$, and extending along φ_2. The probability distribution along the fibers is not constant, it shows maximum values for $\varphi_2 = 0^{\circ}$ or 60° and minimum values for $\varphi_2 = 30^{\circ}$. The orientations having $\varphi_2 = 0^{\circ}$ or $\varphi_2 = 60^{\circ}$ correspond to crystals with their (10-10) plane normal along the RD (c_1 type), whilst those orientations having $\varphi_2 = 30^{\circ}$ correspond to crystals with their (11–20) plane normal along the RD (c_2 type). The main four texture components are schematically represented in Fig. 1-(b) as hexagonal cells in the sample reference system. They have been labelled ${c_1}^{0^{\circ}}$ and ${c_2}^{0^{\circ}}$ for the fibre at $\varphi_1 = 0^{\circ}$, and ${c_1}^{180^{\circ}}$ and ${c_2}^{180^{\circ}}$ for the fibre at $\varphi_1 = 180^{\circ}$. The locations of these ideal texture components in the Euler orientation space are identified in Fig. 1-(c). The origin of these fibers starts at the rolling stage, where grain rotation during deformation yields a fiber texture with intense c_1 and low c_2 components. During subsequent annealing, recrystallization occurs and texture is modified with further increase of c_2 orientations at the expense of c_1 orientations [14].

2.2. Zr2.5%Nb pressure tubes

CANDU nuclear power plants employ 4 mm thick, 6 m long and

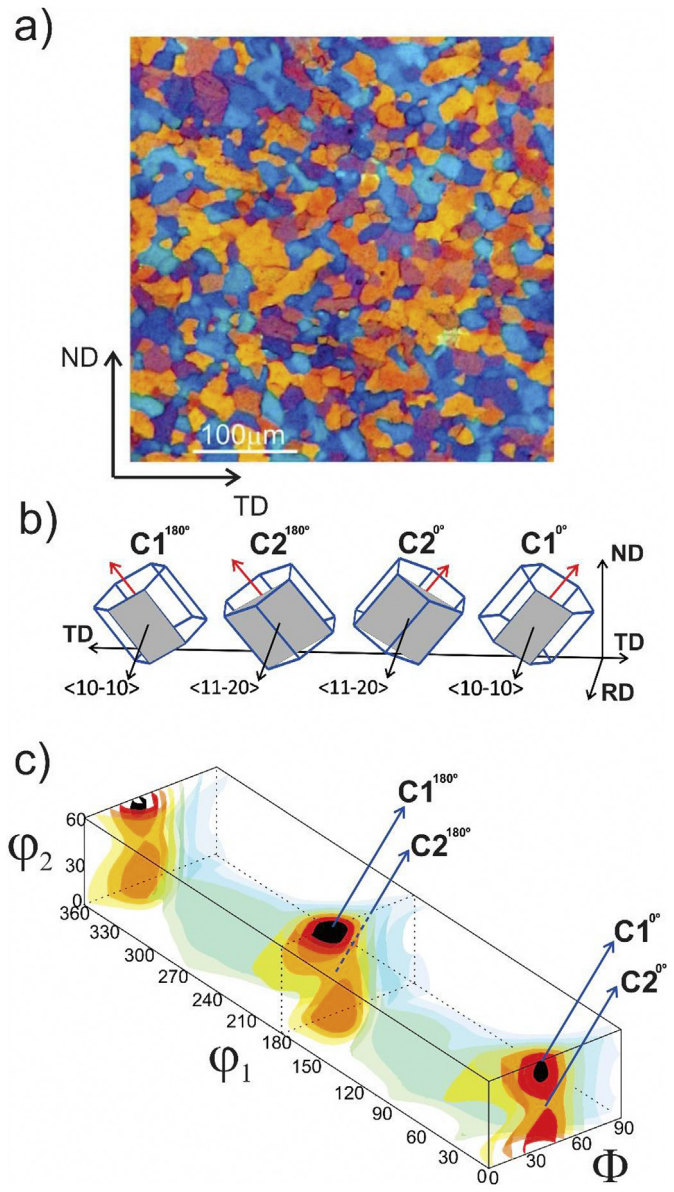

Fig. 1. Microstructural features of warm-rolled Zircaloy-4 plate: a) Polarized light image of the normal-transverse plane, b) Schematic representation of main texture components c) 3D plot of the ODF displaying two fibre like texture with axis at ($\Phi \sim 35°$, $\varphi_1 = 0°$) and ($\Phi \sim 35°$, $\varphi_1 = 180°$, along φ_2. The location of the main texture components discussed in the literature are indicated.

100 mm diameter Zr2.5%Nb pressure tubes that contain the fuel elements and coolant. These tubes are manufactured from Zr2.5% Nb billets forged at ~800 °C. The typical manufacturing procedure (as stated by Atomic Energy Canada Limited, AECL) consists of: 1) an extrusion step at ~800 °C; 2) air cooling down to room temperature; 3) cold drawing (about 20%–30% reduction); 4) a final thermal treatment (autoclaving) at 400 °C for 24 h. The National Atomic Energy Commission of Argentina (CNEA) has successfully implemented a slightly different manufacture process where the cold drawing reduction (step 3) is replaced by a cold-pilger rolling stage [32]. Small specimens were machined out from an experimental Zr2.5%Nb CANDU pressure tube produced at CNEA, with dimensions of ~10 mm × 20 mm along the axial and rolling directions respectively (AD and RD in pole figures).

The mechanical properties and microstructure of Zr2.5%Nb pressure tubes have been extensively studied in the literature [33].

Fig. 2-(a) shows typical TEM image across the radial-axial plane for the present specimens. The ODF has been measured in detail by HE-XRD experiments at the 1-ID beamline of APS, USA [34], and Fig. 2-(c) shows an ODF plotted as a 3D surface in the Euler space. The microstructure consists of lamellar α-grains with an *hcp* crystal structure that contain between 0.6 wt.% to 1 wt.% Nb, surrounded by a grain boundary network composed by Nb-stabilized β-Zr (*bcc* crystal structure, ~18–20 wt.% Nb) and a metastable ω-phase (simple hexagonal structure). The crystallographic texture is strong and is mainly determined at the extrusion stage [35]. The ODF is dominated by crystals having their ⟨10-10⟩ axes along the tube axial direction; and their c-axes distributed between the hoop and radial directions, with a clear maximum along the hoop direction, as schematically represented in Fig. 2-(b). This main texture

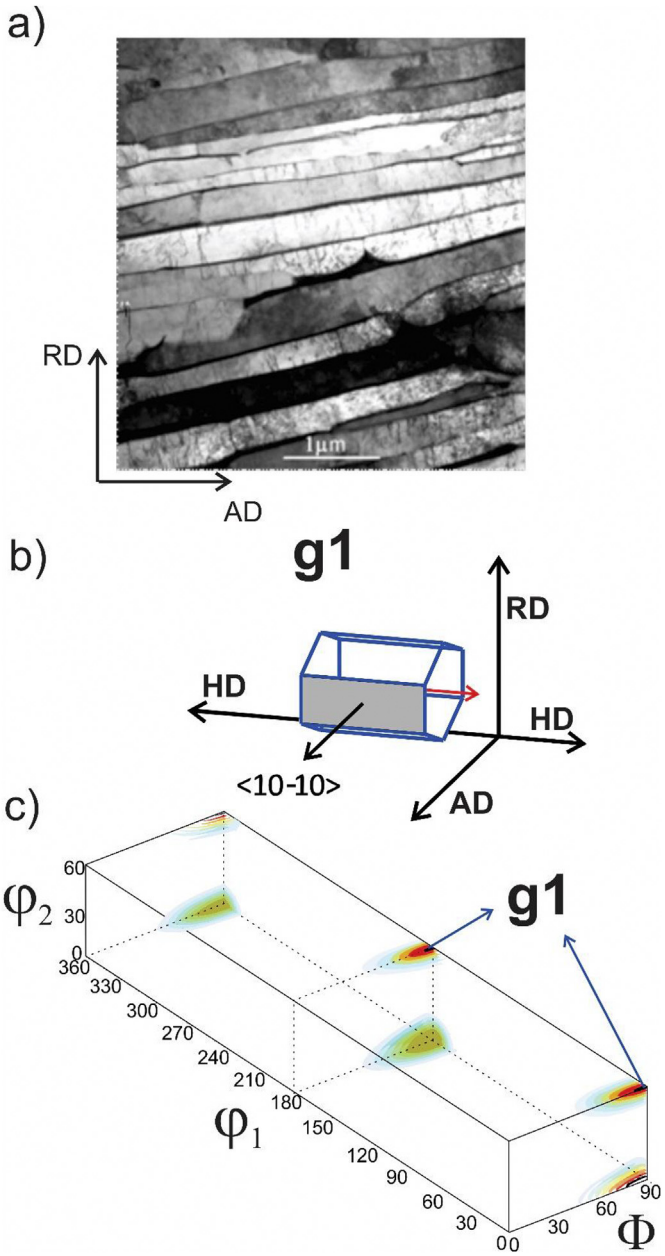

Fig. 2. Zr2.5%Nb pressure tube: a) TEM image (radial-axial plane) b) Schematic representation of the main texture component c) 3D plot of the ODF displaying an intense maxima at $\varphi_1 = 0°$ and $\varphi_1 = 180°$. Also the location of the main texture component g_1 is indicated.

component has Euler angles very close to $\varphi_1 = 0°$, $\Phi = 90°$, and $\varphi_2 = 0°$ or 60° and it has been labelled as g_1 in Fig. 2-(c). By symmetry this component shows another maximum at $\varphi_1 = 180°$, $\Phi = 90°$, $\varphi_2 = 0°$ *or* 60°.

3. Instruments

Three dedicated texture diffractometers (SKAT, HIPPO, CARR-TD), and two residual stress diffractometers (Kowari, ENGIN-X) were used for this round robin exercise. Two of them were constant-wavelength instruments (Kowari, CARR-TD), and three were polychromatic instruments using the time-of-flight (TOF) technique (SKAT, HIPPO, ENGIN-X). Brief descriptions of each of them are given below.

3.1. HIPPO (LANSCE, LANL, USA)

HIPPO is a high flux, medium resolution TOF texture diffractometer with a sample position located at ~9 m from the moderator at the pulsed neutron spallation source of the Los Alamos Neutron Science Center. HIPPO's large detector coverage allow for short count times for quantitative texture analysis (few minutes for single phase steel, Mg, Zr etc. samples) as well as high throughput powder diffraction or kinetic studies [36]. After a reconfiguration in 2011, 53 detector panels with a total of 1200 ^{3}He tubes are arranged on five rings around the incident beam direction with nominal diffraction angles of 40°, 60°, 90°, 120°, and 144°. A ~2 m^3 sample chamber can accommodate ancillary equipment such as a robotic sample changer [37], furnaces, cryostats, or a load frame. Thermal neutron flux at sample is ~10^7 n $cm^{-2}s^{-1}$ [38], typically provided as 10 mm diameter beam spot. The available range of lattice spacing (d) spans from 1.2 Å to 3.5 Å, which allowed measuring 11 reflections simultaneously (from (100) to (202)). Count times for most texture samples on HIPPO are on the order of minutes per orientation with typically three rotations around the vertical axis measured for a full reconstruction of the ODF of Zr alloys.

3.2. SKAT (IBR-2, JINR, Russia)

This is a TOF diffractometer specially designed for measurement of texture in larger geological specimens It is located at a ~103 m long flight path at the end of a bend neutron guide at the IBR-2 pulsed reactor. The selection of water (more suitable for measurements of materials with smaller unit cells such as cubic ot hexagonal metals) or composite − water + cryogenic (for geological samples) moderator is available for the beamline. The standard setup of SKAT has an axi-symmetrical arrangement of 19 ^{3}He detector modules on a single Debye-Scherrer cone at a scattering angle of $2\theta = 90°$, which allows measurements of multiple (due to TOF technique) complete pole figures in 5 × 5° grid [39]. A combination of large beam cross section (50 mm × 90 mm) and Soller-type collimators on detectors (55 mm × 55 mm, 45′ divergence) offers the ability to measure sample volumes over 100 cm^3 with a good angular pole figure resolution (<3°). Flux at the sample is ~10^6 n $cm^{-2}s^{-1}$ [40], and the normally available range of lattice spacing (d) goes from 0.65 Å to 5.25 Å. Typical measurement time (if uniform pole figure coverage is required) is ~1 day. Diffraction spectra of Zr alloy samples were analysed in the interval of $d = 1.02–2.92$ Å, where there are 15 reflections of α-Zr (from (100) to (211)). The HIPPO and SKAT diffractometers were compared in detail in Ref. [41].

3.3. NTD (CARR, CIAE, China)

The Neutron Texture Diffractometer is a constant-wavelength diffractometer located at a thermal neutron beam at the China Advanced Research Reactor (CARR) and it has been specifically designed to measure texture [42]. A vertically bent Cu (111) monochromator directs a 30 × 30 mm^2 neutron beam of 1.48 Å into a sample located at 180 cm from the monochromator, fit into an Eulerian cradle of 40 cm diameter. Pole figures are produced using a single ^{3}He detector tube and a 200 mm × 200 mm, two-dimensional position sensitive detector. Flux at sample is 5.6×10^7 n $cm^{-2}s^{-1}$. Typical counting time per pole figure was 120 min.

3.4. Kowari (OPAL, ANSTO, Australia)

This is a constant-wavelength diffractometer located at a thermal neutron guide specifically designed for measuring residual stresses [43]. The incident wavelength can be varied between 1 Å and 2.4 Å due to the possibility of using a variable take-off angle from a double-focusing bent-perfect crystal Silicon monochromator. Flux at sample is ~7×10^6 n $cm^{-2}s^{-1}$ (depending on incident wavelength). For texture measurements, the radial collimator in front of the detector is removed. The wavelength used for the experiments was 1.8 Å and typical measuring time per sample was 8 h for 6 independent *hkl* pole figures.

3.5. ENGIN-X (ISIS, STFC, UK)

ENGIN-X is a TOF residual stress diffractometer optimized to measure high-resolution diffraction patterns at precise locations deep in the interior of bulk samples [44]. It is located at a ~50 m flight path at the end of a curved guide viewing a methane moderator. It has two diffraction banks at ~1.5 m from the sample position, centred at scattering angles of ±90°, to measure diffraction patterns along two perpendicular directions simultaneously. Each detector bank is composed by 1200 detectors, covering ±16° in the horizontal plane and ±21° in the vertical plane. A single detection bank covers a total detector area of 1.4 m^2, which represents about a 5% of the total 4π solid angle. Flux at sample is ~5×10^6 n $cm^{-2}s^{-1}$. The wavelength range used was 1.8–6.5 Å which allowed measuring 16 reflections with d-spacings between 1 Å and 3 Å simultaneously (from (100) to (114)). Typical counting times per ODF were 30 min using a gauge volume of (6 × 4 × 4) mm^3.

4. Experimental details and ODF analysis

4.1. Pole figure coverage

Specimens were distributed among participants for the determination of direct pole figures (PF). Fig. 3 shows the actual PF experimental grids explored by each instrument in the present experiments. Rather sophisticated PF grids were used for the polychromatic instruments, e.g., SKAT (a), HIPPO (b), and ENGIN-X (c), whilst regularly spaced grids were used by the constant wavelength diffractometers, Kowari (d, 5°x5°) and CARR-NTD (e, 10°x5°). For comparison, the figure also shows the PF grid used for the companion synchrotron HE-XRD experiments performed on 3 mm diameter cylindrical specimens, reported in Refs. [34] and [14],. Those experiments used a 300 × 300 μm^2 beam of 80 keV with the detector on transmission mode, so the beam went through the entire thickness of the sample.

Several complete pole figures were measured at the two constant-wavelength diffractometers. The (10-10), (0002), (10–11), (11–20), (10–13) pole figures were measured at Kowari, whilst only the (10-10) and (0002) pole figures were measured at CARR-NTD.

On the other hand, at the TOF diffractometers several reflections are measured simultaneously for a constant diffraction angle (or sample direction), which must be corrected for several factors

affecting diffraction peak intensities (form factor, multiplicity, incident intensity etc.). As several detectors are used, partial coverage of many pole figures is provided by the specific detector arrangement. In all three TOF instrument, PF coverage was completed by performing a limited number of specimen rotations, rendering the PF grids shown in Fig. 3. Three rotations were used at HIPPO, thirty-five rotations at SKAT, and four rotations at ENGIN-X.

PF coverage was clearly incomplete for ENGIN-X, yet the measurement was considered mostly as a trial for texture determination at TOF residual stress diffractometers. In those instruments,

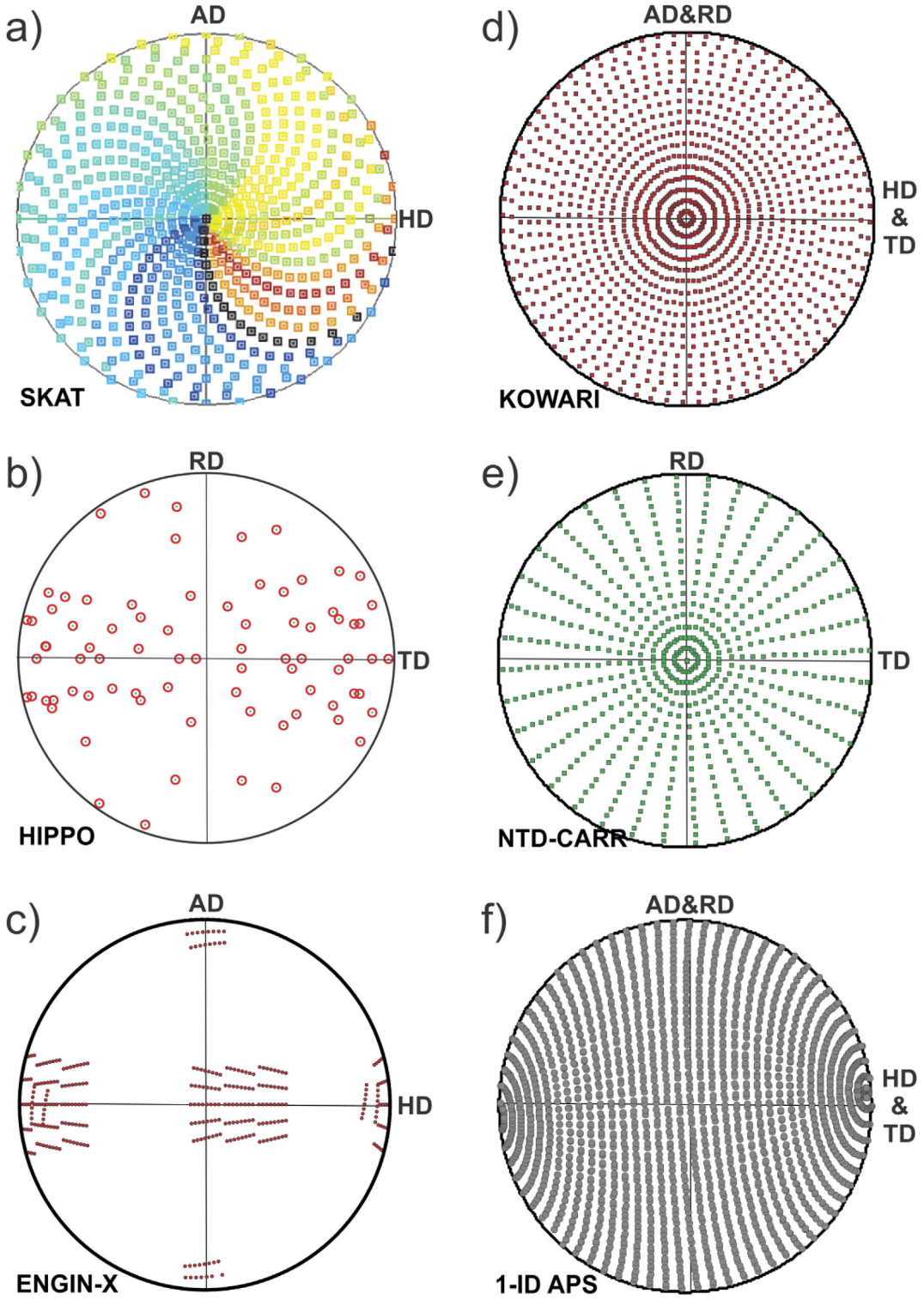

Fig. 3. Zr2.5%Nb pressure tube: a) TEM image (radial-axial plane) b) Schematic representation of the main texture component c) 3D plot of the ODF displaying an intense maxima at $\varphi_1 = 0^\circ$ and $\varphi_1 = 180^\circ$. Also the location of the main texture component g_1 is indicated. Pole figure coverage explored by the experiments at a) SKAT, b) HIPPO, c) ENGINX, d) Kowari, e) CARR-NTD, f) APS (Synchrotron high energy X-ray diffraction). The plotting convention stands: Rolling and Axial direction pointed to north, then: Transverse and Hoop direction pointed to east.

small gauge volumes are used to study bulk components with spatial resolution ($6 \times 4x4$ mm^3 in the present case), yet a limited number of specimen orientations is usually explored due to limitation in beam time availability. In fact, the measurements included here correspond to experiments performed to analyze microstructural variations at different stages of pressure tube production, including not only texture, but also dislocation densities and minor phases [45]. Four orientations and 80 detectors (each one covering ~$2^\circ \times 4^\circ$) rendered a total of 320 points of the PF. Despite the reduced coverage, the ENGIN-X PF grid were focused on the most relevant areas of the Zr2.5%Nb pole figures, in order to sample the important parts of the (0002) and (10-10) pole figures, namely, the radial-hoop line, and the region surrounding of the axial direction. Details of the strategy used for texture measurements and associated data-analysis can be found in Ref. [20]. For the companion HE-XRD experiments 10 experimental pole figures were measured.

4.2. ODF analysis

The experimental pole figures measured at constant wavelength instruments were used to produce the ODF using the MTEX Toolbox in Matlab [24]. The ODF in MTEX is approximated by a superposition of individual components, the exact number, position and width of these components can be specified by the user. In this case, the positions were equally spaced with 5° resolution in the orientation space. Each component was modeled as a de la Vallee Poussin distribution with half widths of 10° and 8°, for Zircaloy-4 and Zr2.5%Nb, respectively. The same procedure was applied to determine the ODF for the companion synchrotron HE-XRD experiments.

Due to the complexity of the detector arrangement and incident beam corrections, pole figure extraction and ODF texture analysis at TOF diffractometers is usually performed by Rietveld-type full pattern refinement software. At SKAT and HIPPO, the ODF was described by the EWIMV method using the code MAUD [26]. The resolution of the ODF calculated in EWIMV was equal to 5° for SKAT and 10° for HIPPO. For presentation and calculation of derived parameters, recalculated pole figures produced by those programs were used as input to define the ODF within the MTEX Toolbox using the same criteria as for the constant wavelength instruments. All ODFs were calculated from experimental or recalculated pole figures without sample symmetries imposed. Table 1 recapitulates technical and experimental information from all neutron instrument and measurement. The Australian diffractometer, Kowari, was the only instrument which measured both samples.

4.3. Quantitative parameters

Several parameters have been used for quantitative comparison of the ODFs produced by the different instruments, as described below.

The texture index t is a parameter used to quantify the texture strength [31], which mathematically represents the integral value of the squared ODF, and is defined as:

$$t = \int f(g)^2 dg \tag{1}$$

where g represents the orientation, and $f(g)$ is the ODF.

As described in the Samples section, the ODF of both specimens can sometimes be synthetically described by mean of a series of ideal orientations; e.g., ($c_1{}^{0^\circ}$, $c_2{}^{0^\circ}$, $c_1{}^{180^\circ}$, $c_2{}^{180^\circ}$) for the Zircaloy-4 plates, and g_1 for the Zr2.5%Nb pressure tubes. A useful parameter for the quantitative assessment of the strength of a specific texture component $g_0 = (\varphi_1^0, \Phi^0, \varphi_2^0)$, is its volume fraction, $V_F(g_0)$. This parameter gives the fraction of crystals in the sample with orientation within a vicinity around the orientation g_0 considering a radius of possible misorientations, r.

$$V_F(g_o) = \int_{g_0-r}^{g_0+r} f(g) dg \tag{2}$$

On the other hand, the actual Euler angles on which an ideal component g_0 is effectively observed are in practice slightly different from the *ideal* values introduced before, $g_0 = (\varphi_1^0, \Phi^0, \varphi_2^0)$. Such actual values can be quantitatively defined by computing the first-order momenta of the measured ODF in the vicinity of g_0, along each of the Euler angles. For the Euler angle φ_1 the *local* first-order momentum, or *centroid*, associated to the ideal g_0 component is calculated as

$$\overline{\varphi}_1(g_o) = \frac{\int_{\varphi_1^0-\Delta\varphi_1}^{\varphi_1^0+\Delta\varphi_1} \varphi_1 f\left(\varphi_1, \Phi^0, \varphi_2^0\right) d\varphi_1}{\int_{\varphi_1^0-\Delta\varphi_1}^{\varphi_1^0+\Delta\varphi_1} f\left(\varphi_1, \Phi^0, \varphi_2^0\right) d\varphi_1} \tag{3}$$

where $\Delta\varphi_1$ defines an interval around φ_1^0 that fully contains that part of the ODF ascribed to the g_0 component. The respective $\overline{\Phi}(g_o)$ and $\overline{\varphi}_2(g_o)$ centroids corresponding to the Φ and φ_2 Euler angles are calculated accordingly.

Following these ideas, the effective *angular width* of a component can be estimated by evaluating the standard deviation along each of the Euler angles. The standard deviation of the Euler angle φ_1 associated to the ideal g_0 component is calculated as

$$[\delta\varphi_1(g_o)]^2 = \frac{\int_{\varphi_1^0-\Delta\varphi_1}^{\varphi_1^0+\Delta\varphi_1} [\varphi_1 - \overline{\varphi}_1(g_o)]^2 f\left(\varphi_1, \Phi^0, \varphi_2^0\right) d\varphi_1}{\int_{\varphi_1^0-\Delta\varphi_1}^{\varphi_1^0+\Delta\varphi_1} f\left(\varphi_1, \Phi^0, \varphi_2^0\right) d\varphi_1} \tag{4}$$

with the same notation as before, and the respective

Table 1
Technical data comparison between instruments and measurement.

Technique	TOF			Constant wavelength	
Instruments	HIPPO	SKAT	ENGIN-X	Kowari	CARR
Source type	Spallation	Pulse reactor	Spallation	Reactor	Reactor
Samples	Zry-4	Zr2.5Nb	Zr2.5Nb	Zr2.5Nb & Zry-4	Zry-4
Incident beam cross section (maximum)	20 *mm* diam.	50 *x* 90 *mm*^{2}	10 *x* 30 *mm*^{2}	< 25 *mm* diam.	30 *x* 30 *mm*^{2}
Neutron flux (n/cm^2 s)	~ 10^7	~ 10^6	~ 5 10^6	~ 7 10^6	~ 5.6 10^7
Detector	1360 ^{3}*He*	19 ^{3}*He*	1200 scintill.	2D ^{3}*He*	Single ^{3}*He*
N° of measured points per PF	108	665	320	1296	648
N° of reflections included in analysis	> 10	> 10	5	5	2

$\delta\Phi(g_o)$ and $\delta\varphi_2(g_o)$ standard deviations corresponding to the Φ and φ_2 Euler angles are calculated accordingly. These standard deviations can be used as guidance for the definition of the misorientations radius r to be adopted in the evaluation of the volume fraction of a component, as given by Eq. (2).

In the case of hexagonal materials, a parameter commonly used by designers to quantitatively specify texture requirements is the Kearns factor [46]. This parameter could be used to estimate the values of a physical property along different principal axes of the sample, if that property of interest has different values along the c-axis and in the basal plane of the hexagonal single crystals composing polycrystalline sample. The Kearns factor along the principal sample axis z is calculated as

$$f_z = \int_0^{\frac{\pi}{2}} I_{(0002)}(\beta)\sin\beta\cos^2\beta d\beta \tag{5}$$

where $I_{(0002)}(\beta)$ is the average (0002) pole figure intensity at an angle β from that direction.

Good correlation has been reported between the texture parameters defined above and mechanical properties of the material (yield stress, ultimate elongation, etc.), with the local centroids of the ODF being the parameters displaying the highest correlation factors [47]. For all ODFs measured by different instruments, we have evaluated texture indices, volume fractions, local first and second momenta of the main texture components, and Kearns factors using the MTEX Toolbox.

5. Results

5.1. Zircaloy-4 plates

Neutron diffraction experiments on the Zircaloy-4 specimens were performed at the instruments Kowari, HIPPO, and NTD. Fig. 4 shows recalculated pole figures, and ODF sections for $\varphi_1 = 0°$ and $\varphi_1 = 180°$ obtained for all instruments. Results from HE-XRD experiments measured at beamline 1-ID of APS are also included for comparison. Good agreement is found both qualitatively and

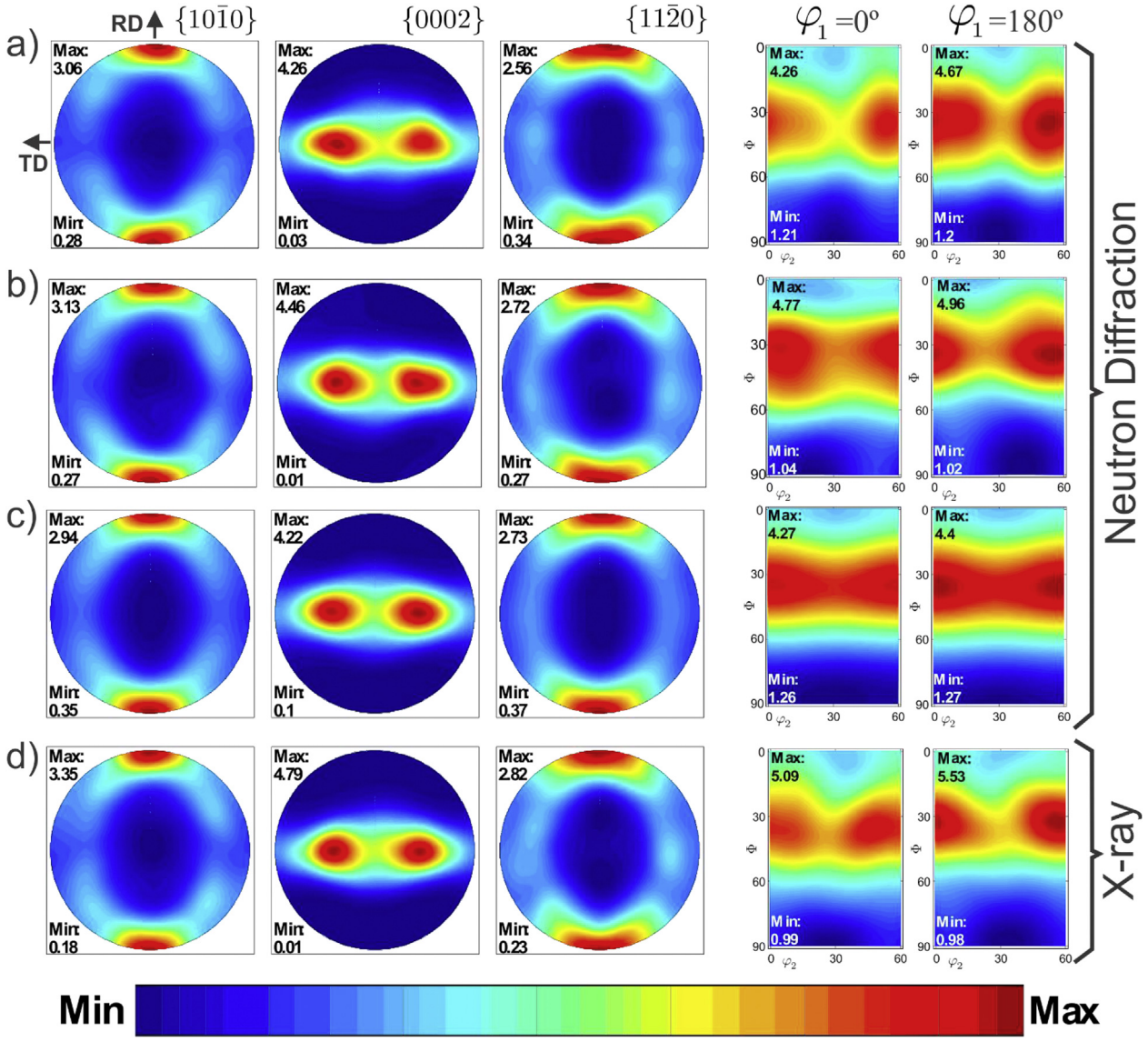

Fig. 4. Recalculated pole figures and $\varphi_1 = 0°$, 180° ODF sections for Zircaloy-4 specimens measured at a) HIPPO, b) KOWARI, c) NTD, d) 1-ID at APS (High-Energy X-ray diffraction). The plotting convention stands: Rolling direction pointed to north,: Transverse direction pointed to east.

Table 2
Kearns factors, texture index t and parameters of the main texture component for the Zircaloy-4 specimen, measured by the different instruments participating in this study.

Instrument	ODF	c_1^{180} component					c_2^{180} component					Kearns Factors			
	t	V_F(%)	$\overline{\Phi}$(°)	$\delta\Phi$(°)	$\overline{\varphi_1}$(°)	$\delta\varphi_1$(°)	V_F(%)	$\overline{\Phi}$(°)	$\delta\Phi$(°)	$\overline{\varphi_1}$(°)	$\delta\varphi_1$(°)	Transverse	Normal	Rolling	Sum
Kowari	2.3	4.7	38.5	22.6	179.8	28.2	4.1	37.6	22.7	179.7	28.9	0.359	0.553	0.086	0.998
HIPPO	2.2	4.5	39.7	22.9	179.2	28.4	3.8	39.4	22.9	178.8	29.1	0.365	0.55	0.084	0.999
NTD	2.1	4.2	39.3	22.7	177.6	28.6	3.9	39.8	22.8	177.6	28.8	0.361	0.538	0.099	0.998
1-ID APS	2.5	5.1	38.7	22.6	180.8	27.5	4.2	38.6	22.3	181.4	28.3	0.351	0.577	0.071	0.999
Average $\bar{x}$	2.28	4.63	39.05	22.70	179.35	28.18	4.00	38.85	22.68	179.38	28.78	0.359	0.555	0.085	0.999
St. Dev σ	0.11	0.26	0.51	0.13	1.05	0.28	0.14	0.96	0.15	1.1	0.20	0.004	0.010	0.008	0.001
$\sigma/\bar{x}$ (%)	4.87	5.61	1.31	0.57	0.58	0.99	3.54	2.47	0.66	0.61	0.70	1.02	1.79	9.56	0.05

quantitatively among the different neutron instruments, as well as with the companion HE-XRD experiments. In particular, all pole figures show rather symmetric pole figures, yet the ODF reveal asymmetries on the TD-ND line, with the $\varphi_1 = 180°$ fibre slightly more intense than the $\varphi_1 = 0°$ fibre.

For more quantitative comparison, Table 2 lists the derived Kearns factors, texture indexes t, centroids and angular widths of the ideal texture components of the fibre found at $\varphi_1 = 180°$, e.g., c_1^{180} and c_2^{180} (described in Section 2.1 and schematically represented in Fig. 1-b). For all parameters, the table includes the values for each instrument together with the arithmetic average ($\bar{x}$) and the associated standard deviation (σ). The last row of the table gives an estimation of the relative uncertainty to be expected for each of the parameters when measured at a neutron diffractometer (for this particular material). In doing this, we have consider that σ provides an experimental first-order estimate of such uncertainty.

The average texture index measured by the neutron experiments is t=(2.28 ± 0.08), where we have used $\sigma/\sqrt{2}$ for the uncertainty of the average. The value differs in ~10% from the value obtained from HE-XRD experiments. Typical uncertainty to be expected for t for a single neutron experiment is ~5%. On the other hand, Kearns factors present average values of f_{TD}=(0.359 ± 0.003), f_{ND}=(0.555 ± 0.007), and f_{RD}=(0.085 ± 0.006), for the transverse, normal and rolling directions, respectively. Measurement precision for the non-negligible Kearns factors is better than for texture indexes, as the uncertainties σ_{TD}~0.004 and σ_{ND}~0.01 represent percentages of ~1% and ~2%, respectively. These uncertainties must be compared to the differences of ~3% and ~5% with the results of the companion HE-XRD experiments. The main reason behind the scatter observed in the Kearns factors reported by different neutron instruments is most likely due to uncertainties in the alignment of the specimen. In order to estimate the impact of sample misalignement on Kearns factors, we deliberately introduced a 5° misalignment in the adopted data analysis chain. We obtained numerical differences of ~ 0.008 between the Kearns factors evaluated with and without misalignement. The difference with the HE-XRD results is most likely due to the through thickness variation of the ODF across the specimens, and the different size of the volumes gauged by the two techniques.

Fig. 5 presents detailed comparisons of the ODFs obtained for the different instruments along selected lines that provides fine details of the fibres, and allows quantification of angular position and width for two of its main components, c_1^{180} and c_2^{180} (please, see Fig. 1-c for overall reference). In all cases, the actual lines of the ODF being compared are shown as white dotted lines in the 2D sections of the ODF shown in the insets. Fig. 5-a and 5-b characterizes the width and position of the fibre in the φ_2 and Φ axes, respectively, whilst Fig. 5-c shows the distribution of orientations along the fibre. More precisely, Fig. 5-a shows the lines $(\varphi_1,\ \Phi = 35°, \varphi_2 = 0°)$ and $(\varphi_1, \Phi = 35°, \varphi_2 = 30°)$ that have been used to calculate the centroid and standard deviation $(\overline{\varphi_1}, \delta\varphi_1)$ of the c_1^{180} and c_2^{180} components listed in Table 2. Similarly Fig. 5-b shows the lines $(\varphi_1 = 180°,\ \Phi, \varphi_2 = 0°)$ and $(\varphi_1 = 180°,\ \Phi, \varphi_2 = 30°)$, used to calculate the centroid and standard deviation $(\overline{\Phi}, \delta\Phi)$ of the c_1^{180} and c_2^{180} components, respectively. As seen in the figure, the line profiles for all instruments present similar features, with higher maximum intensities of the ODF for the c_1^{180} texture component (4–5.5 m. r.d), than for the c_2^{180} component (3.5–4.1 m. r.d). In particular, all three neutron diffractometers presents similar shapes, whilst the companion HE-XRD results display a more prominent maximum at c_1^{180}. The maximum ODF values change less than 15% among the neutron diffractometers. From Table 2, we observe that the angle corresponding to the maximum of the distributions are all within ±1.5° of the theoretical c_1^{180} orientation ($\varphi_1 = 180°,\ \Phi = 35°,\ \varphi_2 = 0°$) and within ±2.2° of the theoretical c_2^{180} orientation ($\varphi_1 = 180°,\ \Phi = 35°,\ \varphi_2 = 30°$). The second momenta are very similar for both components, $\delta\Phi$=$(22.7 \pm 0.1)°$ and $\delta\varphi_1$~$(28.5 \pm 0.3)°$. Overall, the angular widths of the components are ~30° along Φ and ~50° along φ_1. Based on this we have adopted a misorientation radius r of 15° to evaluate the volume fractions, which resulted in average values of (4.6 ± 0.2)% and (4.0 ± 0.1)% for c_1^{180} and c_2^{180} components, respectively, where again we have used $\sigma/\sqrt{2}$ for the uncertainty of the average.

On the other hand, Fig. 5-c reveals a clear variation in intensity along the fibre, which are less pronounced for NTD-CARR results. This is likely to be due to slightly incomplete experimental information, as only two pole figures were measured in this instrument, and hence the ODF cannot reproduce the intensity variations along the fibre, as observed in the other cases.

5.2. Zr2.5%Nb pressure tubes

Experiments on the Zr2.5%Nb specimens have been performed at Kowari, SKAT and ENGIN-X instruments. Fig. 6 shows recalculated pole figures and $\varphi_2 = 0°$ sections of the experimental ODF obtained for each case. Results from HE-XRD experiments measured at beamline 1-ID of APS are also included for comparison. Again, rather good qualitative and quantitative agreement is found among the instruments, yet some minor differences emerge in the trial ENGIN-X measurements. For better comparison, Table 3 lists the derived Kearns factors, texture indexes t, centroids and angular widths for g_1, the ideal texture component described in Section 2.2 and schematically represented in Fig. 2-(b). For all parameters the table includes the average ($\bar{x}$) and standard deviation (σ) evaluated without including the trial ENGIN-X measurements, as we intend to assess the uncertainty of such fast measurement strategy. As before, we consider the evaluated standard deviation (including the companion HE-XRD measurement) as the typical uncertainty to be expected from a single measurement.

The average texture index of the pressure tubes, $t = 6.8 \pm 0.2$, is considerable larger than that of the Zircaloy-4 plates ($t = 2.28 \pm 0.08$), as expected from the comparison of the ODFs

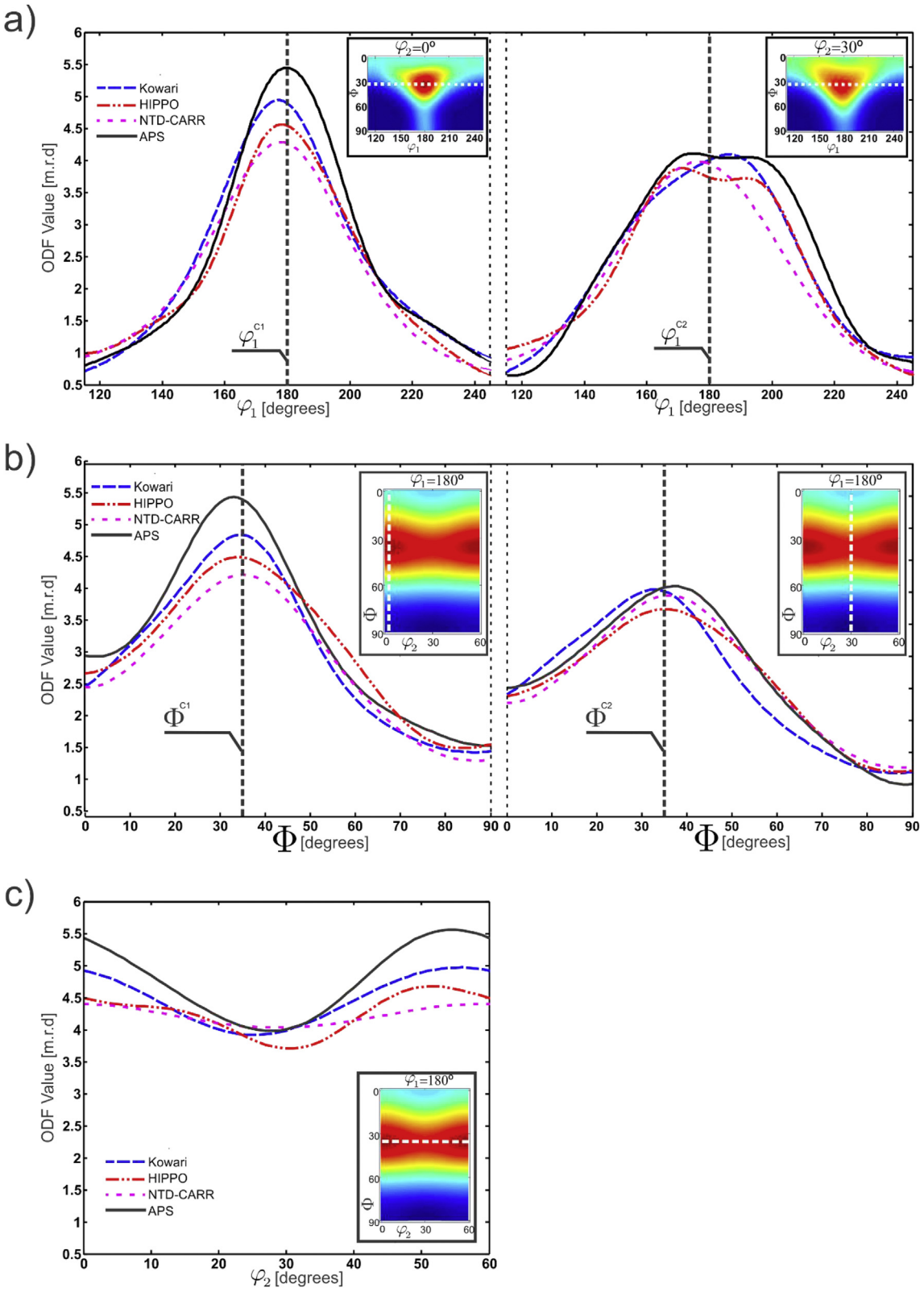

Fig. 5. Line profiles of the ODF for Zircaloy-4 warm rolled plate specimens. The profiles correspond to the dashed lines shown in the insets.

presented in Fig. 1-(c) and 2-(c). Fine details of the pressure tube ODF are presented in the line profiles shown in Fig. 7, which allow quantification of the angular position and width of the g_1 component along the three Euler angles. As before, the actual lines of the ODF being compared are shown as white dotted lines in the 2D sections of the ODF shown in the insets. Fig. 7-(a) and 7-(c) corresponds to the lines across φ_1 and φ_2, and have been used to calculate the values $(\overline{\varphi}_1, \delta\varphi_1)$ and $(\overline{\varphi}_2, \delta\varphi_2)$ listed in Table 3, whilst

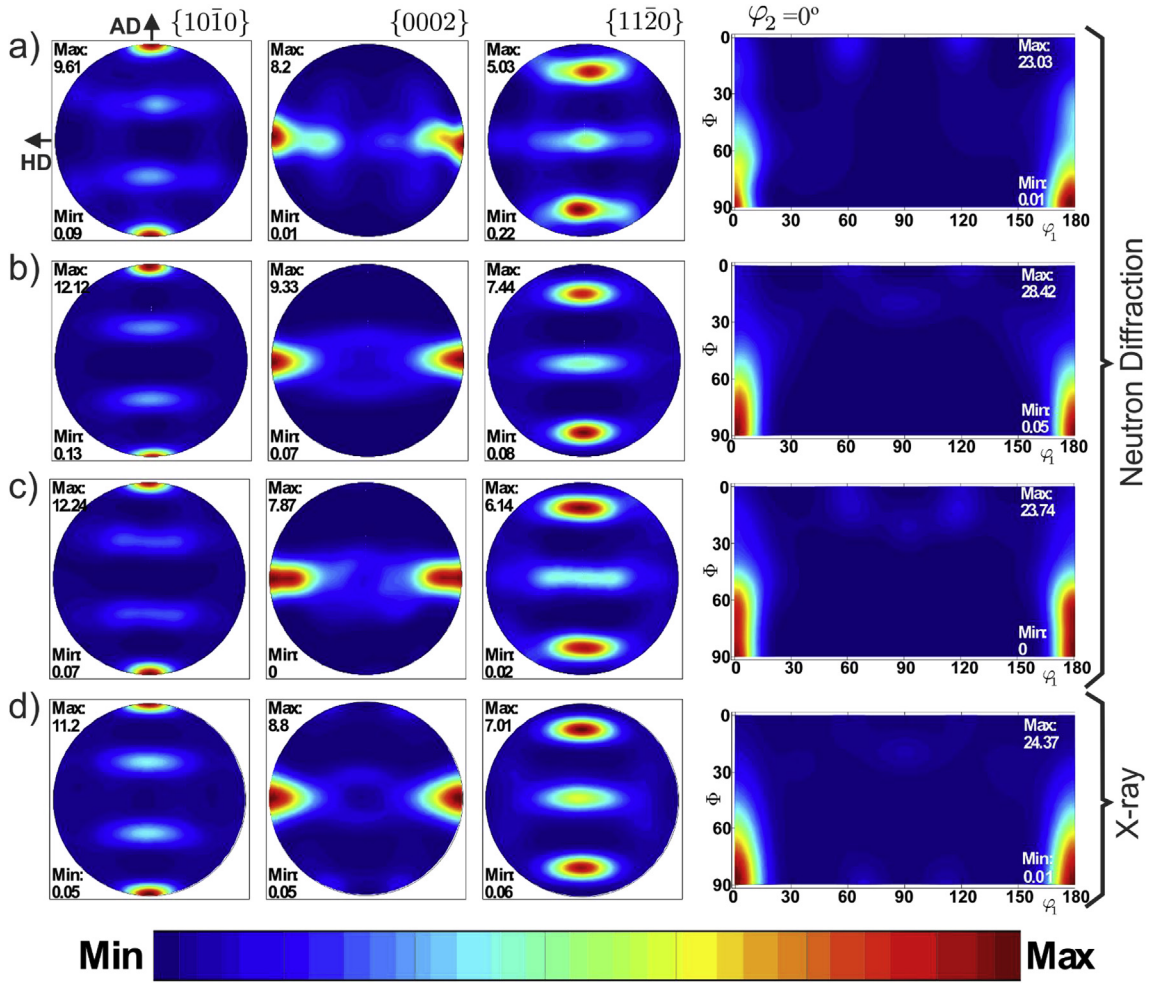

Fig. 6. Recalculated pole figures and $\varphi_2 = 0°$ ODF sections for the Zr2.5%Nb specimens measured at a) ENGIN-X, b) SKAT, c) KOWARI, d) 1-ID at APS (High-Energy X-ray diffraction). The plotting convention stands: Axial direction pointed to north, Hoop direction pointed to east.

Table 3
Kearns factors, texture index and ODF data for the Zr2.5%Nb specimen.

Instrument	ODF	g_1 component							Kearns Factors		
	t	V_F(%)	$\overline{\varphi}_1$	$\delta\varphi_1$	$\overline{\Phi}$	$\delta\Phi$	$\overline{\varphi}_2$	$\delta\varphi_2$	Hoop	Radial	Axial
SKAT	7.0	6.9	180.8	9.2	91.1	32.7	57.4	8.1	0.553	0.341	0.103
Kowari	7.9	6.4	179.7	7.4	91.3	34.8	59.0	8.06	0.598	0.355	0.043
EnginX	4.4	5.4	177.3	10.5	89.9	38.3	60.1	9.4	0.580	0.335	0.083
1-ID APS	6.5	6.5	180.2	8.7	89.5	28.1	61.6	7.6	0.567	0.353	0.077
Statistics (without ENGIN-X)											
Average $\bar{x}$	7.1	6.6	180.2	8.4	90.6	31.9	59.3	7.9	0.573	0.350	0.074
St. Dev σ	0.7	0.3	0.6	0.9	1.0	3.4	2.1	0.3	0.023	0.008	0.030
$\sigma/\bar{x}$ (%)	9.9	4.0	0.3	11.0	1.1	10.8	3.6	3.5	4.0	2.2	40.5
EnginX-$\bar{x}$ (%)	38.3	18.2	1.6	−24.5	0.8	−20.2	−1.3	−18.7	−1.3	4.2	−11.7

Fig. 7-(b) shows the fiber-like distribution found along Φ. As seen in the figure, the profiles from all instruments look reasonably similar, and maximum ODF values in Zr2.5%Nb pressure tube material ~30 are considerable larger than those of Zircaloy-4 plates (~5, Fig. 5). Average positions of the g_1 component, $\overline{\varphi}_1$=(180.2 ± 0.6), $\overline{\Phi}$=(90.6 ± 1.0) and $\overline{\varphi}_2$=(59.3 ± 2) are very close to the ideal values $\varphi_1 = 180°$, $\Phi = 90°$, and $\varphi_2 = 60°$. The FWHM of the g_1 component along φ_1 and φ_2 are comparable, 20.0° and 18.6° respectively, as estimated from the measured values of $\delta\varphi_1$ and $\delta\varphi_2$ (FWHM~2.35 $\delta\varphi$). A much wider, fiber-like distribution is observed along Φ, over a range of ±45° around Φ~90°. Typical uncertainties for the position and width of the distributions are ~2° and ~3°, respectively. Based on the measured widths, the volume fractions of the g_1 component were calculated using a sphere radius of 15°. The average volume fraction measured by the different instruments is (6.6 ± 0.3)%.

On the other hand, Kearns factors present average values of f_H=(0.573 ± 0.02), f_R=(0.350 ± 0.008), and f_A=(0.074 ± 0.03), which expected uncertainties of 4%, 2% and 40%, respectively. As before, the experimental standard deviation for the non-negligible Kearns factors (~0.03), is of the same order of magnitude as the numerically estimated uncertainty (~0.01) by considering the effect of

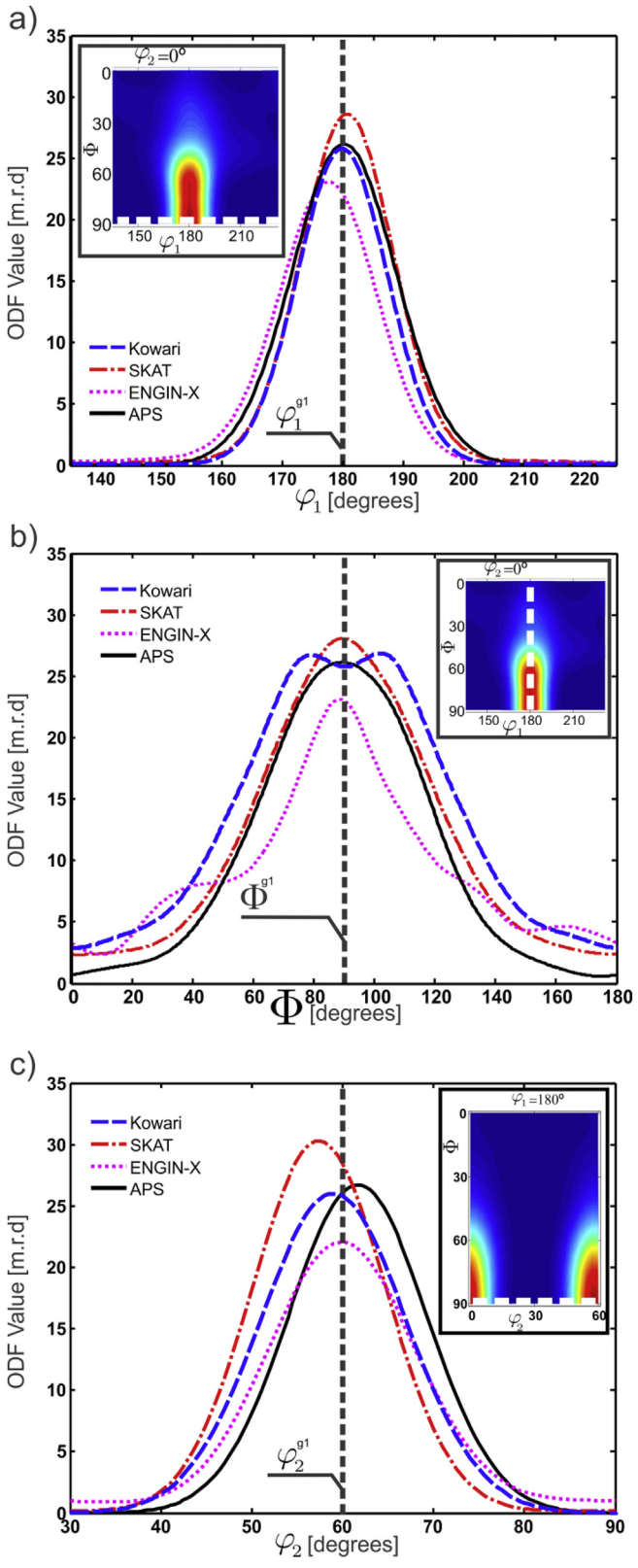

Fig. 7. Line profiles of the ODF for Zr2.5Nb pressure tube specimens. The profiles correspond to the dashed lines shown in the insets.

specimen misalignment (~5°). Within this uncertainty the Kearns factor values obtained for SKAT and Kowari show good agreement, as well as with the companion synchrotron HE-XRD experiment.

Regarding the trial ENGIN-X measurements, the results in Figs. 6 and 7 show that the reduced pole figure coverage shown in Fig. 3-(c) captures quite well the essential features of the ODF. However, the quantitative parameters listed in Table 3 reveal that, except for the values of the centroids of the g1 distribution ($\overline{\Phi}$, $\overline{\varphi}_2$) the parameters derived from the ENGIN-X ODF are close but still outside of the uncertainty interval defined by the other instruments. However, it must be mentioned that the trial ENGIN-X measurement defines Kearns factors within a 5% uncertainty of the average values.

6. Texture variations in experimental Zr2.5Nb pressure tubes

In order to compare the observed uncertainties in texture parameters determined by neutron diffractometers with typical texture variations found in manufacturing, we have measured the ODF of different batches of pressure tubes produced by CNEA (labelled A, B, C, D and E). Measurements were performed at the SKAT neutron diffractometer on specimens produced from the front and back sections of cold-rolled tubes.

Fig. 8 shows the comparisons of the ODFs obtained for front and back specimens of different batches along the same lines as in Fig. 7 (shown as dotted lines in the insets). Overall, rather large variations are observed in the maximum ODF's values (21–33 m. r.d) among the different specimens for both front and back sets. Relatively large variations are also observed in the centroid of the φ_2 distribution for the front of the tubes (Fig. 8-(c)) and of the width of the Φ distribution for the back of the tubes (Fig. 8-(b)).

Table 4 provides more quantitative comparisons, in terms of the derived Kearns factors, texture indexes t, centroids and angular widths for the ideal texture component g_1. The table list the values obtained for each sample, together with separate statistical parameters ($\overline{x}$, σ) of front and back groups. The bottom section of the table presents statistical parameters considering the complete set of specimens, in order to estimate average values for the tubes.

The texture indices measured for the front samples give an average value of (6.5 ± 0.3), ~18% lower than the average value of (7.8 ± 0.3) for the back samples. The difference between front and back is considerable larger than the statistical uncertainty (~4%), which itself is very close to the instrumental uncertainty estimated in the previous section. The position of the φ_2 centroid for the front samples (Fig. 8-c), $\overline{\varphi}_2 = (60.4 \pm 1.3)^\circ$, is ~3% different to that of the back samples, $\overline{\varphi}_2 = (58.7 \pm 0.6)^\circ$. The width of the Φ distribution for the back samples (Fig. 8-b), $\delta\Phi = (34.7 \pm 0.6)$, is slightly larger than that of the front samples, $\delta\Phi = (36.2 \pm 1.0)$. On the other hand, average values of radial and hoop Kearns factors for front and back groups differ only by ~0.5%, and can be considered as identical, based on the standard deviation observed within each group (>2%). The same observation is valid for the axial Kearns factor, yet with much larger percentual difference and uncertainties involved. Statistical averages for the whole batch give values of $f_H = (0.569 \pm 0.004)$, $f_R = (0.345 \pm 0.003)$, and $f_A = (0.085 \pm 0.003)$, with standard deviations of ~2%, ~3% and ~10%, respectively. These results are consistent with the Kearns factor values obtained for the same samples by laboratory X-ray diffraction measurements [48]. Estimated volume fractions of the g_1 component for samples from the front and back section also agree, and give an overall average value of $V_F = (6.4 \pm 0.3)\%$.

7. Discussion

As seen in Figs. 4–7, we have found good overall agreement,

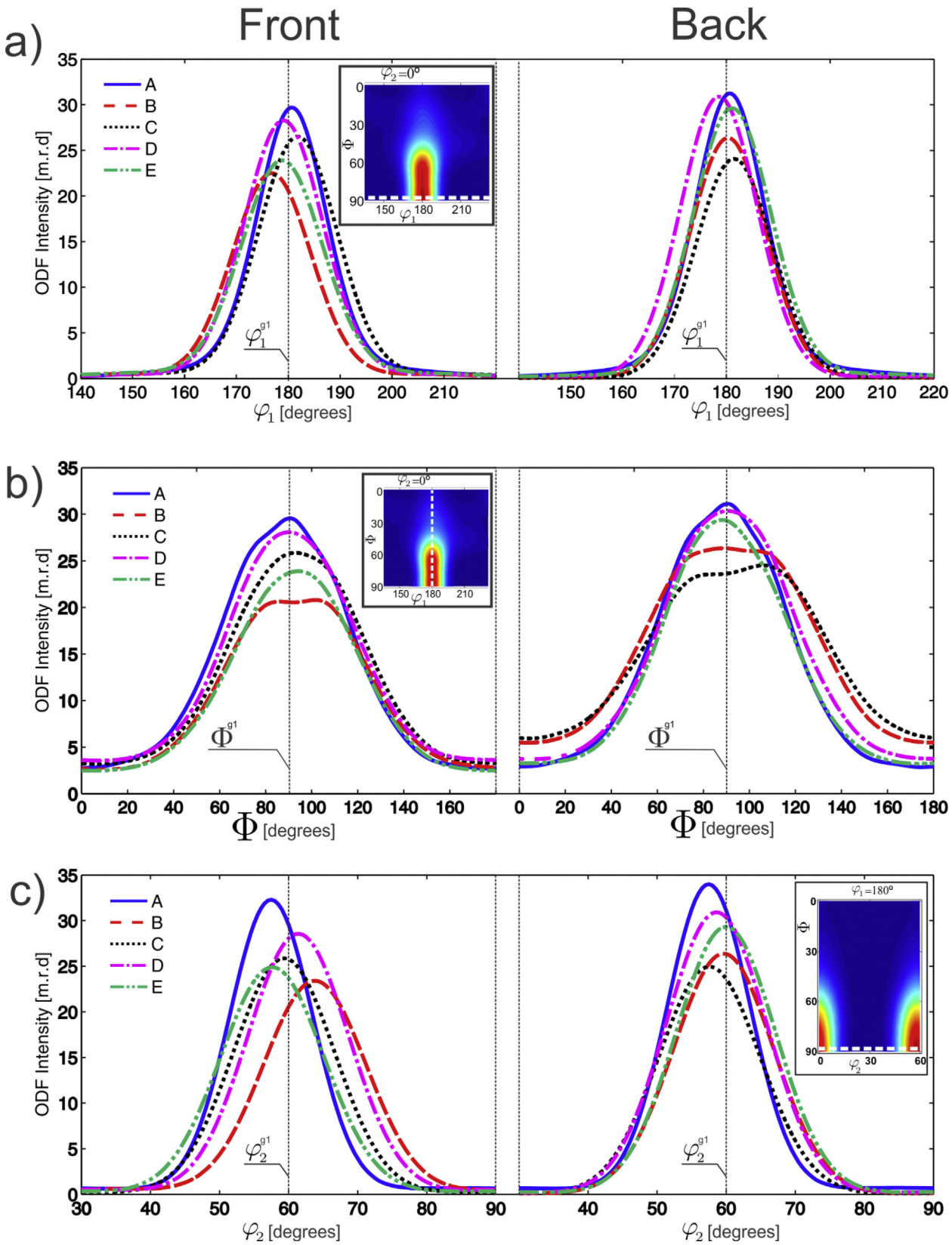

Fig. 8. Line profiles of the ODF for different batches of Zr2.5Nb pressure tubes for front (a) and back (b) specimens.

Table 4
Kearns factors, texture index and ODF data for different batches of pressure tubes.

Sample		ODF	g_1 component							Kearns Factors		
		t	V_F(%)	φ_1	$\delta\varphi_1$	Φ	$\delta\Phi$	$\overline{\varphi}_2$	$\delta\varphi_2$	Hoop	Radial	Axial
Front	A	7	6.5	180.8	9.2	91.1	32.7	57.4	8.1	0.553	0.341	0.103
	B	6.4	5.4	176.9	9.6	92.6	35.2	63.4	8.4	0.575	0.345	0.079
	C	6.4	6.2	181.7	9.5	92.7	34.9	59.3	7.7	0.562	0.351	0.085
	D	6.9	6.8	179.1	9.1	91	34.8	61.3	8.0	0.581	0.332	0.085
	E	5.7	5.9	178.9	10	92.1	33.7	57.8	8.0	0.557	0.349	0.093
	Average $\overline{x}$	6.5	6.2	179.5	9.5	92.1	34.7	60.4	8.0	0.569	0.344	0.086
	St. Dev σ	0.5	0.6	1.9	0.3	0.8	1.1	2.6	0.3	0.012	0.008	0.010
	$\sigma/\overline{x}$ (%)	8.0	9.0	1.0	3.6	0.9	3.3	4.3	3.3	2.2	2.2	11.8
Back	A	7.7	6.9	180.5	8.3	88.7	33.1	57.7	7.4	0.567	0.344	0.088
	B	7.9	6.3	180.4	7.8	91.2	38.8	59.6	7.4	0.565	0.354	0.080
	C	8.1	5.8	181.5	7.8	92.7	40.4	57.6	7.4	0.564	0.363	0.073
	D	8.2	7.3	178.6	8.2	90.9	34.8	58.6	7.5	0.592	0.333	0.072
	E	7.0	7.0	181.2	9.0	89.8	33.9	59.9	7.5	0.573	0.336	0.089
	Average $\overline{x}$	7.8	6.7	180.4	8.2	90.7	36.2	58.7	7.5	0.572	0.346	0.080
	St. Dev σ	0.5	0.6	1.1	0.5	1.5	3.2	1.1	0.1	0.012	0.012	0.008
	$\sigma/\overline{x}$ (%)	6.4	8.9	0.6	5.8	1.7	8.9	1.8	0.7	2.1	3.6	10.2
	Front-Back (%)	−18.2	−7.8	−0.5	14.7	1.5	−4.2	2.9	6.5	−0.5	−0.6	7.2
Overall	Average $\overline{x}$	7.1	6.4	180	8.8	91.3	35.2	59.3	7.7	0.569	0.345	0.085
	St. Dev σ	0.8	0.6	1.5	0.8	1.3	2.5	1.9	0.3	0.012	0.010	0.009
	$\sigma/\overline{x}$ (%)	11.7	9.4	0.9	8.6	1.4	7.1	3.2	4.5	2.1	2.8	11.1

both qualitatively and quantitatively, among bulk textures determined in Zircaloy-4 plates and Zr2.5%Nb pressure tubes at five neutron diffractometers worldwide. These instruments were considerably different in their specific design and in pole figure coverage, as exemplified in Section 3 and Fig. 3.

For quantitative comparison we used *overall* parameters that sample the whole ODF (texture index and Kearns factors); and *local* parameters that characterize the basic features of the most important components of the ODF (centroids, angular widths, and volume fractions of individual components).

The characteristic uncertainties to be expected in the values of these parameters from measurements performed at a neutron diffractometer were roughly estimated as the standard deviation of the values obtained by different instruments. For overall parameters, the uncertainty observed for non-negligible Kearns factors (f_T~1% and f_N~2% in Zircaloy-4; f_H~1.5% and f_R~3% for Zr2.5%Nb) is better than the uncertainty in texture index (~5% in Zircaloy-4 plates, ~10% in Zr2.5%Nb). For local parameters, the uncertainty in the position of the centroid of individual texture components (~1% both in Zircaloy-4 and Zr2.5%Nb) is considerably better than the uncertainty in the associated volume fractions (~5% in Zircaloy-4, 10% in Zr2.5%Nb). The absolute uncertainty in Kearns factors measured for Zircaloy-4 plates was <0.01, which due to similarities in microstructure can be compared to the results of a X-ray diffraction texture Round Robin on a stress-relieved Zircaloy-4 fuel cladding with 14 participants [9]. The standard deviation in Kearns factors was larger in that case, ~0.06, likely due to the smaller volumes gauged by the X-ray technique and the slightly more complex preparation of the specimens. In particular, the Kearns factors measured for the transverse, normal and rolling directions of the Zircaloy-4 plate of this work are comparable to the corresponding values reported in the Zircaloy-4 fuel cladding Round Robin: $f_T = 0.30–0.36$. $f_N = 0.54–0.66$. $f_R = 0.03–0.09$. On the other hand. the Kearns factors measured for the Zr2.5%Nb pressure tube compare well with values obtained by laboratory X-ray diffraction on samples from a different batch of the same material, $f_H = 0.53–0.56$, $f_R = 0.34–0.39$, $f_A = 0.06–0.10$ [48].

The main reason behind the observed scatter in the Kearns factors is very likely to be due uncertainties in the production and alignement of the specimens, which has been estimated in ~5°. This explanation is consistent with the variations observed in those parameters when misalignments in sample orientation are introduced in the calculation chain. For the same reason, a similar uncertainty is expected in the values obtained by high-energy synchrotron X-ray diffraction reported in Refs. [7,32] which were included for comparison in Tables 2 and 3 Hence, the reported uncertainties are considered as upper bounds and could be in principle reduced by detailed manufacturing and alignment of the samples.

An additional source of uncertainty comes from the reported differences in pole figure coverage. This includes not only the numbers of pole figures and the density of orientations explored, but also the specific orientations probed by the experiment. This would certainly be an issue when the number of measured pole figures (or reflections) is < 3 or when the pole figure coverage fails to sample all relevant portions of the pole figure. The latter issue was clearly observed in the trial ENGIN-X experiments, which showed a value of texture index ~35% off from the average value. However, this approach should not be discarded, as by means of a relatively fast (<30 min), spatially resolved ($4 \times 4x6$ mm^3), non-destructive texture measurement centroids of the distribution were defined with an uncertainty <2°, and Kearns factors with an uncertainty <5%. In this sense, it would be useful to determine minimum pole figure coverage that is necessary to bring the results within the typical uncertainties reported here.

A final source of uncertainty not discussed here may come from the specific mathematical method used to calculate the complete ODF (Spherical Harmonics, EWIMV, MTEX). Here, we have used MTEX to model the ODF, starting from pole figures, either experimental (constant wavelength instruments and ENGIN-X), or recalculated from the EWIMV-derived ODF (HIPPO and SKAT, using the MAUD package).

Finally, the measurements performed on the back and front sections of a batch of cold-rolled Zr2.5%Nb pressure tubes experimentally confirmed that the typical uncertainty achieved in neutron diffractometers is very suitable to characterize typical

variations appearing in the development and tailoring of Zr-alloy tube manufacturing processes.

8. Conclusions

A small round robin on specimens from Zircaloy-4 plates and Zr2.5%Nb pressure tubes has shown that the crystallographic texture of common Zr alloys can be precisely quantified in neutron diffractometers worldwide, with little sample preparation required, despite large differences in instrument design and pole figure coverage. Typical uncertainty expected in global texture parameters is ~5% in texture index, and ~2% in relevant Kearns factors.

Main synthetic texture components can be defined in terms of angular position, angular width and volume fractions with typical uncertainties of ~1%, ~5% and ~4%, respectively.

The reported precision is adequate for typical variations found across and between specimens during development and optimization of manufacturing processes.

Uncertainties in the production and alignement of the specimens seems to be the main reason behind the standard deviation in the integral parameters of the ODF reported by different instruments.

Acknowledgments

The authors wish to thank Dr. Alberto Baruj for fruitful discussions. This research was partially funded by CONICET under PIP 11220110100542. and by IAEA under Research Contract 17252.

Appendix A. Supplementary data

Supplementary data related to this article can be found at https://doi.org/10.1016/j.jnucmat.2018.08.003.

References

[1] E. Tenckhoff, Deformation Mechanisms, Texture, and Anisotropy in Zirconium and Zircaloy, ASTM International, 1988.
[2] A.V. Flores, A.G. Gomez, G.A. Juarez, N. Loureiro, R.I. Samper, J.R. Santisteban, M.A.V. Alvarez, A. Tolley, A. Condó, R.D. Bianchi, A.D. Banchik, P. Vizcaíno, Typical zirconium alloys microstructures in nuclear components, Pract. Metallogr. 51 (2014) 656–674, https://doi.org/10.3139/147.110304.
[3] D.K. Rodgers, C.E. Coleman, M. Griffiths, G.A. Bickel, J.R. Theaker, I. Muir, A.A. Bahurmuz, S.S. Lawrence, M. Resta Levi, In-reactor performance of pressure tubes in CANDU reactors, J. Nucl. Mater. 383 (2008) 22–27, https://doi.org/10.1016/j.jnucmat.2008.08.037.
[4] J.A. Szpunar, W. Qin, H. Li, N.A.P. Kiran Kumar, Roles of texture in controlling oxidation, hydrogen ingress and hydride formation in Zr alloys, J. Nucl. Mater. 427 (2012) 343–349, https://doi.org/10.1016/j.jnucmat.2012.05.005.
[5] P. Vizcaíno, J.R. Santisteban, M.A. Vicente Alvarez, A.D. Banchik, J. Almer, Effect of crystallite orientation and external stress on hydride precipitation and dissolution in Zr2.5%Nb, J. Nucl. Mater. 447 (2014) 82–93, https://doi.org/10.1016/j.jnucmat.2013.12.025.
[6] M.A. Vicente Alvarez, J.R. Santisteban, P. Vizcaino, A.V. Flores, A.D. Banchik, J. Almer, Hydride reorientation in Zr2.5Nb studied by synchrotron X-ray diffraction, Acta Mater. 60 (2012) 6892–6906, https://doi.org/10.1016/j.actamat.2012.07.029.
[7] J.R. Santisteban, M.A. Vicente-Alvarez, P. Vizcaíno, A.D. Banchik, J.D. Almer, Hydride precipitation and stresses in zircaloy-4 observed by synchrotron X-ray diffraction, Acta Mater. 58 (2010) 6609–6618, https://doi.org/10.1016/j.actamat.2010.08.022.
[8] K.B. Colas, A.T. Motta, J.D. Almer, M.R. Daymond, M. Kerr, A.D. Banchik, P. Vizcaino, J.R. Santisteban, In situ study of hydride precipitation kinetics and re-orientation in Zircaloy using synchrotron radiation, Acta Mater. 58 (2010) 6575–6583, https://doi.org/10.1016/j.actamat.2010.07.018.
[9] J.E. Lewis, G. Schoenberger, R.B. Adamson, B.A. Cheadle, H. Stehle, E. Tenckhoff, G. Baro, E.D. Hindle, Texture Measurement Techniques for Zircaloy Cladding: a Round-robin Study, ASTM Spec. Tech. Publ., 1982, pp. 39–62.
[10] V.V. Sumin, I.V. Papushkin, R.N. Vasin, A.M. Venter, A.M. Balagurov, Determination of the residual stress tensor in textured zirconium alloy by neutron diffraction, J. Nucl. Mater. 421 (2012) 64–72, https://doi.org/10.1016/j.jnucmat.2011.11.053.
[11] L. Balogh, D.W. Brown, P. Mosbrucker, F. Long, M.R. Daymond, Dislocation structure evolution induced by irradiation and plastic deformation in the Zr–2.5Nb nuclear structural material determined by neutron diffraction line profile analysis, Acta Mater. 60 (2012) 5567–5577, https://doi.org/10.1016/j.actamat.2012.06.062.
[12] H.M. Reiche, S.C. Vogel, P. Mosbrucker, E.J. Larson, M.R. Daymond, A furnace with rotating load frame for in situ high temperature deformation and creep experiments in a neutron diffraction beam line, Rev. Sci. Instrum. 83 (2012) 053901, https://doi.org/10.1063/1.4708619.
[13] H.-R. Wenk, I. Lonardelli, D. Williams, Texture changes in the hcp → bcc → hcp transformation of zirconium studied in situ by neutron diffraction, Acta Mater. 52 (2004) 1899–1907, https://doi.org/10.1016/j.actamat.2003.12.029.
[14] A. Moya Riffo, M.A. Vicente Alvarez, J.R. Santisteban, P. Vizcaino, S. Limandri, M.R. Daymond, D. Kerr, J. Okasinski, J. Almer, S.C. Vogel, Crystallographic texture and microstructural changes in fusion welds of recrystallized Zry-4 rolled plates, J. Nucl. Mater. 488 (2017) 83–99, https://doi.org/10.1016/j.jnucmat.2017.02.015.
[15] C. Mareau, M.R. Daymond, Comparison of experimentally determined texture development in Zircaloy-2 with predictions from a rate-dependent polycrystalline model, Mater. Sci. Eng. 528 (2011) 8676–8686, https://doi.org/10.1016/j.msea.2011.08.040.
[16] H. Abdolvand, M.R. Daymond, Internal strain and texture development during twinning: comparing neutron diffraction measurements with crystal plasticity finite-element approaches, Acta Mater. 60 (2012) 2240–2248, https://doi.org/10.1016/j.actamat.2012.01.016.
[17] H. Abdolvand, M.R. Daymond, Multi-scale modeling and experimental study of twin inception and propagation in hexagonal close-packed materials using a crystal plasticity finite element approach—Part I: average behavior, J. Mech. Phys. Solid. 61 (2013) 783–802, https://doi.org/10.1016/j.jmps.2012.10.013.
[18] M.R. Daymond, R.A. Holt, S. Cai, P. Mosbrucker, S.C. Vogel, Texture inheritance and variant selection through an hcp–bcc–hcp phase transformation, Acta Mater. 58 (2010) 4053–4066, https://doi.org/10.1016/j.actamat.2010.03.012.
[19] R.W.L. Fong, R. Miller, H.J. Saari, S.C. Vogel, Crystallographic texture and volume fraction of α and β phases in Zr-2.5Nb pressure tube material during heating and cooling, Metall. Mater. Trans. 43 (2012) 806–821, https://doi.org/10.1007/s11661-011-0914-6.
[20] F. Malamud, J.R. Santisteban, V. Alvarez, R. Bolmaro, J. Kelleher, S. Kabra, W. Kockelmann, Texture analysis with a time-of-flight neutron strain scanner, J. Appl. Crystallogr. 47 (2014) 1337–1354.
[21] H.-G. Brokmeier, W.M. Gan, C. Randau, M. Völler, J. Rebelo-Kornmeier, M. Hofmann, Texture analysis at neutron diffractometer STRESS-SPEC, Nucl. Instrum. Methods Phys. Res. Sect. Accel. Spectrometers Detect. Assoc. Equip. 642 (2011) 87–92, https://doi.org/10.1016/j.nima.2011.04.008.
[22] F. Malamud, S. Northover, J. James, P. Northover, S. Nneji, J. Kelleher, Spatially resolved texture analysis of Napoleonic War era copper bolts, J. Appl. Crystallogr. 50 (2017), https://doi.org/10.1107/S1600576717011761.
[23] U.F. Kocks, Texture and Anisotropy: Preferred Orientations in Polycrystals and Their Effect on Materials Properties, Cambridge University Press, 2000.
[24] R. Hielscher, H. Schaeben, A novel pole figure inversion method: specification of the MTEX algorithm, J. Appl. Crystallogr. 41 (2008) 1024–1037, https://doi.org/10.1107/S0021889808030112.
[25] R.B. Von Dreele, Quantitative texture analysis by Rietveld refinement, J. Appl. Crystallogr. 30 (1997) 517–525, https://doi.org/10.1107/S0021889897005918.
[26] S. Matthies, L. Lutteroti, H.R. Wenk, Advances in texture analysis from diffraction spectra, J. Appl. Crystallogr. 30 (1997) 31–42, https://doi.org/10.1107/S0021889896006851.
[27] H.-R. Wenk, Standard project for pole-figure determination by neutron diffraction, J. Appl. Crystallogr. 24 (1991) 920–927, https://doi.org/10.1107/S0021889891004661.
[28] J.R. Santisteban, F. Malamud, P. Vizcaino, M.J. Li, S.C. Vogel, P. Liaw, D.G. Carr, V.I. Sumin, R. Vasin, Preliminary Round Robin on the Determination of Crystallographic Texture of ZR Components by Neutron Diffraction, 2015. http://inis.iaea.org/Search/search.aspx?orig_q=RN:47013673.
[29] I.A.E. Agency, Use of Neutron Beams for Materials Research Relevant to the Nuclear Energy Sector. Annex: Individual Reports, International Atomic Energy Agency, 2015. http://inis.iaea.org/Search/search.aspx?orig_q=RN:47013665.
[30] O. Zanellato, The Open University, 2009.
[31] H.J. Bunge, Texture Analysis in Materials Science: Mathematical Methods, Butterworths, 1982.
[32] A.D. Banchik, R.D. Bianchi, P. Vizcaíno, A.V. Flores, W.C. Szieber, L.J. Galeta, A.G. Gómez, Tecnología de Fabricación de Componentes Estructurales del Núcleo base Circonio para Reactores Nucleares de Potencia, CNEA, 2009.
[33] Assessment and Management of Ageing of Major Nuclear Power Plant Components Important to Safety: CANDU Pressure Tubes, IAEA, Vienna, 1998. http://www-pub.iaea.org/MTCD/Publications/PDF/te_1037_prn.pdf.
[34] M.A. Vicente Alvarez, J.R. Santisteban, G. Domizzi, J. Almer, Phase and texture analysis of a hydride blister in a Zr–2.5%Nb tube by synchrotron X-ray diffraction, Acta Mater. 59 (2011) 2210–2220, https://doi.org/10.1016/j.actamat.2010.12.024.
[35] R.A. Holt, S.A. Aldridge, Effect of extrusion variables on crystallographic texture of Zr-2.5 wt% Nb, J. Nucl. Mater. 135 (1985) 246–259, https://doi.org/10.1016/0022-3115(85)90084-4.
[36] H.-R. Wenk, L. Lutterotti, S. Vogel, Texture analysis with the new HIPPO TOF diffractometer, Nucl. Instrum. Methods Phys. Res. Sect. Accel. Spectrometers Detect. Assoc. Equip. 515 (2003) 575–588, https://doi.org/10.1016/

j.nima.2003.05.001.
[37] A.S. Losko, S.C. Vogel, H.M. Reiche, H. Nakotte, A six-axis robotic sample changer for high-throughput neutron powder diffraction and texture measurements, J. Appl. Crystallogr. 47 (2014) 2109–2112, https://doi.org/10.1107/S1600576714021797.
[38] T. Ino, M. Ooi, Y. Kiyanagi, Y. Kasugai, F. Maekawa, H. Takada, G. Muhrer, E.J. Pitcher, G.J. Russell, Measurement of neutron beam characteristics at the Manuel Lujan Jr. neutron scattering center, Nucl. Instrum. Methods Phys. Res. Sect. Accel. Spectrometers Detect. Assoc. Equip. 525 (2004) 496–510, https://doi.org/10.1016/j.nima.2004.02.003.
[39] K. Ullemeyer, P. Spalthoff, J. Heinitz, N.N. Isakov, A.N. Nikitin, K. Weber, The SKAT texture diffractometer at the pulsed reactor IBR-2 at Dubna: experimental layout and first measurements, Nucl. Instrum. Methods Phys. Res. Sect. Accel. Spectrometers Detect. Assoc. Equip. 412 (1998) 80–88, https://doi.org/10.1016/S0168-9002(98)00340-4.
[40] R. Keppler, K. Ullemeyer, J.H. Behrmann, M. Stipp, Potential of full pattern fit methods for the texture analysis of geological materials: implications from texture measurements at the recently upgraded neutron time-of-flight diffractometer SKAT, J. Appl. Crystallogr. 47 (2014) 1520–1534, https://doi.org/10.1107/S1600576714015830.
[41] H.-R. Wenk, R.N. Vasin, H. Kern, S. Matthies, S.C. Vogel, T.I. Ivankina, Revisiting elastic anisotropy of biotite gneiss from the Outokumpu scientific drill hole based on new texture measurements and texture-based velocity calculations, Tectonophysics 570 (2012) 123–134, https://doi.org/10.1016/j.tecto.2012.06.023.
[42] M.-J. Li, X.-L. Liu, Y.-T. Liu, G.-F. Tian, J.-B. Gao, Z.-X. Yu, Y.-Q. Li, Li-Qi Wu, L.-F. Yang, K. Sun, H.-L. Wang, J.R. Santisteban, D.-F. Chen, The neutron texture diffractometer at the China Advanced Research Reactor, Chin. Phys. C 40 (2016), https://doi.org/10.1088/1674-1137/40/3/036002, 036002.
[43] A. Brule, O. Kirstein, Residual stress diffractometer KOWARI at the Australian research reactor OPAL: status of the project, Phys. B Condens. Matter 385–386 (2) (2006) 1040–1042, https://doi.org/10.1016/j.physb.2006.05.333.
[44] J.R. Santisteban, M.R. Daymond, J.A. James, L. Edwards, ENGIN-X: a third-generation neutron strain scanner, J. Appl. Crystallogr. 39 (2006) 812–825, https://doi.org/10.1107/S0021889806042245.
[45] J.R. Santisteban, P. Vizcaíno, M.Á. Vicente Álvarez, F. Malamud, A. Tartaglione, Crystallographic Phases, Texture and Dislocation Densities of Zr2.5%Nb Pressure Tubes at Different Stages of Manufacturing, IAEA, Vienna, Austria, 2014.
[46] J. Kearns, On the relationship among `f' texture factors for the principal planes of zirconium, hafnium and titanium alloys, J. Nucl. Mater. 299 (2001) 171–174, https://doi.org/10.1016/S0022-3115(01)00686-9.
[47] J.M. Dahl, R.W. McKenzie, J.H. Schemel, Thermomechanical control of texture and tensile properties of Zircaloy-4 plate, Zircon, Nucl. Appl. (1974), https://doi.org/10.1520/STP32110S.
[48] C. Buioli, Textura cristalina de componentes estructurales nucleares de aleaciones en base circonio, Universidad Nacional de Buenos Aires, 2013.